AGU ADVANCING EARTH AND SPACE SCIENCE

JGR Space Physics

RESEARCH ARTICLE
10.1029/2021JA029290

Key Points:

- ESWs corresponding to electron holes appear near the separatrices only on the magnetosphere side during asymmetric reconnection
- When there is no guide field, ESWs are generated by electron two-stream instability
- When there is a guide field, ESWs with distinct phase speed are generated by electron two-stream instability and Buneman instability

Correspondence to:
K. Huang and Q. Lu,
inhk@ustc.edu.cn;
qmlu@ustc.edu.cn

Citation:
Chang, C., Huang, K., Lu, Q., Sang, L., Lu, S., Wang, R., et al. (2021). Particle-in-cell simulations of electrostatic solitary waves in asymmetric magnetic reconnection. *Journal of Geophysical Research: Space Physics*, *126*, e2021JA029290. https://doi.org/10.1029/2021JA029290

Received 26 FEB 2021
Accepted 23 JUN 2021

Particle-In-Cell Simulations of Electrostatic Solitary Waves in Asymmetric Magnetic Reconnection

Cong Chang[1,2], Kai Huang[1,2], Quanming Lu[1,2], Longlong Sang[1,2], San Lu[1,2], Rongsheng Wang[1,2], Xinliang Gao[1,2], and Shui Wang[1,2]

[1]School of Earth and Space Sciences, CAS Key Lab of Geospace Environment, University of Science and Technology of China, Hefei, China, [2]CAS Center for Excellence in Comparative Planetology, Hefei, China

Abstract Electrostatic solitary waves (ESWs) are ubiquitously observed in magnetic reconnection. In this study, two-dimensional (2-D) particle-in-cell (PIC) simulations are performed to investigate the characteristics of ESWs in asymmetric magnetic reconnection. ESWs with bipolar structures of the parallel electric field can be generated near the separatrices only on the magnetosphere side, and propagate to reconnection downstream direction along the magnetic field. These structures corresponding to electron phase-space holes (electron holes) can cross both the electron outflow and inflow channels although their main part is located in the electron outflow. When there is no guide field, the ESWs are generated by electron two-stream instability. When there is a guide field, the amplitude of the ESWs are different on the right and left side of the X line. On the left side, the ESWs are weaker and generated by the electron two-stream instability. On the right side, the ESWs are stronger, and there are two kinds of ESWs with distinct phase speed. The faster one is generated by electron two-stream instability, while the slower one is generated by Buneman instability.

1. Introduction

Magnetic reconnection is an important physical process with the topological change of the magnetic field lines and the conversion of magnetic energy into plasma kinetic energy (Angelopoulos et al., 2013, 2020; Burch et al., 2016; Genestreti et al., 2017; Lu et al., 2013; Parker, 1957; Wang & Lu, 2019; Yamada et al., 2010). The fact that magnetic reconnection can provide sources of free energy for various plasma waves has been demonstrated by satellite observations. These waves can cause strong electron scattering, which may result in the expedition of fast reconnection (Dokgo et al., 2019; Drake et al., 2003; Graham, Vaivads, et al., 2016; Sato & Hayashi, 1979; Wilder et al., 2017; Zhang et al., 2019). Therefore, plasma wave activities are considered to have a significant impact on magnetic reconnection.

A variety of plasma waves have been observed by satellites during magnetic reconnection, including Langmuir waves (Vaivads et al., 2004), lower hybrid waves (Webster et al., 2018; Zhou et al., 2009), electron cyclotron waves (Viberg et al., 2013), electrostatic solitary waves (ESWs) (Cattell et al., 2005; Fujimoto et al., 2011; Lotekar et al., 2020), whistler waves (Graham, Vaivads, et al., 2016; Tang et al., 2013), kinetic Alfvén waves (Chaston et al., 2005). ESWs are known as isolated bipolar spikes in the parallel electric field, which are frequently observed in the diffusion region. Simulation studies indicate that ESWs are related to electron phase-space holes (electron holes) (Huang et al., 2014; Lapenta et al., 2011), which may be generated in the nonlinear stage of the electron stream instability or Buneman instability (Che et al., 2010; Drake et al., 2003; Fujimoto, 2014; Fujimoto & Machida, 2006; Huang et al., 2014; Lu, Wang & Dou, 2005; Lu, Wang, & Wang, 2005; Omura et al., 1996). Matsumoto et al. (2003) reported the first observation of ESWs associated with magnetic reconnection near the magnetosphere side of the dayside magnetopause. The high-resolution observations with Cluster and MMS satellites indicated that ESWs are closely related to the electron beams produced in magnetic reconnection, and can be detected near the separatrices of magnetic reconnection (Cattell et al., 2005; Graham et al., 2015; Graham, Khotyaintsev, et al., 2016; Khotyaintsev et al., 2010; Liu et al., 2019; Retinò et al., 2006; Tong et al., 2018; Viberg et al., 2013). Graham et al. (2015) showed that ESWs detected near the separatrices move at distinct speeds and have distinct spatial scales, and suggested that these ESWs with distinct speeds are caused by different plasma instabilities.

Numerous kinetic simulations have been devoted to study the generation mechanisms of ESWs in magnetic reconnection. Through a three-dimensional (3-D) particle-in-cell (PIC) simulation, Drake et al. (2003) found that the Buneman instability is unstable in the vicinity of the X line during magnetic reconnection with a strong guiding field, and ESWs are at last generated during the nonlinear stage of the instability. Lapenta et al. (2010) demonstrated that the Buneman instability can also be excited and then evolve into ESWs near the separatrices of guide field reconnection, while the electron bump-on-tail instability results in the generation of ESWs near separatrices of both the anti-parallel reconnection and guided field reconnection (Huang et al., 2014; Lapenta et al., 2011; Pritchett, 2004). All these simulations are implemented in symmetric reconnection, where the two inflow regions have the same plasma conditions. Recently, by surveying plasma waves at the dayside magnetopause reconnection, Wilder et al. (2016) found that most of wave activities, including ESWs, are confined in the magnetosphere side with a larger magnetic field and smaller plasma density. In this study, by performing two-dimensional (2-D) PIC simulations, we study the detailed characteristics of ESWs near the separatrices of asymmetric reconnection, the influence of the guide field is also studied.

2. Simulation Model

We use 2-D PIC code where the electric and magnetic fields are updated by the Maxwell equation with an explicit leapfrog algorithm and the particle motions are determined by the Newton-Lorentz equations. Previous researches have shown that the code can be used to study magnetic reconnection and the excitation of plasma waves (Fu et al., 2006; Lu, Wang & Dou, 2005; Lu, Wang, & Wang, 2005; Sang et al., 2018, 2019). The initial magnetic field is $\boldsymbol{B}(z) = B_0\left[\tanh(z/\lambda) + R\right]\boldsymbol{e_x} + B_{y0}\boldsymbol{e_y}$, where λ is the half thickness of the current sheet, B_0 and B_{y0} are the strength of the typical magnetic field and guide field, and the parameter R determines the asymmetry of the magnetic field. The expression of the number density is $n = n_0\left[1 - \alpha_1 tanh(z/\lambda) - \alpha_2\, tanh^2(z/\lambda)\right]$. The pressure balance condition requires the total pressure $n(T_{i0} + T_{e0}) + B_0^2/2\mu_0$ to be constant, where T_{e0} and T_{i0} are the initial temperatures for electrons and ions, respectively, we can get $\alpha_1 = 2R\alpha_2$ and $\alpha_2 = B_0^2/[2\mu_0 n_0(T_{i0} + T_{e0})]$. In our simulations, we choose $R = 1/5$, $T_{i0} = 4T_{e0}$, $\alpha_1 = 2/9$, $\alpha_2 = 5/9$, the variation in magnetic field is from $1.2\,B_0$ to $-0.8B_0$, and the variation in the number density is from $2/9n_0$ to $1/3n_0$, from the magnetosphere side to the magnetosheath side. λ is set to $\lambda = 0.5d_i$(where $d_i = c/\omega_{pi}$ is the ion inertial length based on n_0). Both the ion and electron velocity distributions are assumed to be Maxwellian. The mass ratio m_i/m_e is set to be 100, and the light speed is $c = 15\,V_A$ (where V_A is the Alfven speed, which is calculated with B_0 and n_0). The simulation domain size is $L_x \times L_z = 80d_i \times 40d_i$ with the spatial resolution $\Delta x = \Delta z = 0.05d_i$. The time step is $\Delta t = 0.001\,\Omega_i^{-1}$(Where $\Omega_i = eB_0/m_i$ is the ion gyrofrequency). The number of particles we employ in each species exceeds 10^9. Periodic boundary condition is assumed in the x direction, while in the z direction, we use conducting boundary condition. To make a quick reconnection onset, we assume that the initial flux function has a small disturbance $\Delta\psi = \psi_0 cosh^{-2}(2z/\lambda)cosh^{-2}(x/2)$ and $\psi_0 = 0.1cB_0/\omega_{pi}$.

3. Simulation Results

Two cases are studied in this study: Case 1 is anti-parallel reconnection without a guide field, and Case 2 is asymmetric reconnection with a guide field $B_{y0} = B_0$. Figure 1 presents the parallel electric field $E_\parallel$ (where $E_\parallel = \boldsymbol{E} \cdot \boldsymbol{B}'/|\boldsymbol{B}'|$, $\boldsymbol{B}' = B_x\boldsymbol{e}_x + B_z\boldsymbol{e}_z$ is the in-plane magnetic field) at $\Omega_i t$ = (a) 15, (b) 24, (b) 29, and (d) 34.8 in Case 1. Here, the magnetic field lines are superimposed on the figure. Reconnection onset occurs at about $\Omega_i t$=15, and the parallel electric field begins to appear around the X line. At about $\Omega_i t$= 24, the parallel electric field with bipolar structures begins to develop near the separatrices on the magnetospheric side. Then, the bipolar structures become stronger and stronger, and reach their peak amplitude at about $\Omega_i t$= 29. These structures can exist until the end of the simulation ($\Omega_i t$ =35).

Figure 2 illustrates (a) the parallel electron bulk velocity $V_{e\parallel}$ (where $V_{e\parallel} = \boldsymbol{V}_e \cdot \boldsymbol{B}'/|\boldsymbol{B}'|$ and $\boldsymbol{V}_e$ is the electron bulk velocity) and (b) the electron bulk velocity in the y direction V_{ey} at $\Omega_i t$ =29 for Case 1, at that time $E_\parallel$ near the separatrices has the maximum amplitude. We can find that the electron bulk velocity V_{ey} in the $-y$ direction has a peak value about $3.0V_A$, which is due to the electrons get acceleration around the electron

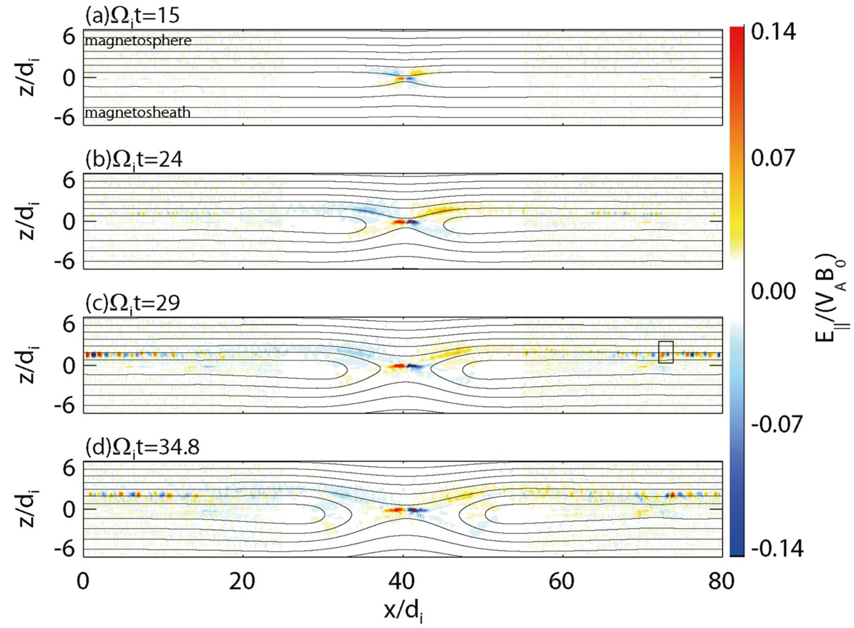

Figure 1. The parallel electric field $E_{\parallel}$ (where $E_{\parallel} = \boldsymbol{E} \cdot \boldsymbol{B}' / |\boldsymbol{B}'|$, and $\boldsymbol{B}' = B_x \boldsymbol{i}_x + B_z \boldsymbol{i}_z$ is the in-plane magnetic field) at $\Omega_i t$ = (a) 15, (b) 24, (b) 29, and (d) 34.8 for Case 1.

diffusion region. These accelerated electrons form the electron outflow jets (denoted by β in Figure 2a) just below the separatrices on the magnetosphere side. Simultaneously, the electron inflow (denoted by α and γ in in Figure 2a) appears near the separatrices on both the magnetosphere and magnetosheath sides.

In order to identify the exact location of the bipolar structures of $E_{\parallel}$ on the magnetosphere side, we plot the distributions of electron bulk velocity $\bar{V}_{e\parallel}$ and the parallel electric field $\left|\tilde{E}_{\parallel}\right|$ versus z at $\Omega_i t = 29$, which are presented in Figure 3. Here, $\left|\tilde{E}_{\parallel}\right|$ $(\bar{V}_{e\parallel})$ at a definite z is the average value of $|E_{\parallel}|$ $(V_{e\parallel})$ at $72\,d_i \leq x \leq 73.8\,d_i$ (as denoted with a rectangle in Figure 1c). Here, the boundary between the inflow and outflow channels of electron is represented by the horizontal red dashed line. The electron inflow is located above the dashed line, while the electron outflow is located below the dashed line. From the figure, we can find that the layer of enhanced $\left|\tilde{E}_{\parallel}\right|$ ranges from the electron outflow channel to the inflow channel, and the half width of this layer is about $0.5d_i$. The peak value of $\left|\tilde{E}_{\parallel}\right|$ is located in the electron outflow region.

Figure 4 exhibits (a) the electron phase-space distribution versus x and $v_{e\parallel}$, and (b) the parallel electric field $\bar{E}_{\parallel}$ at $\Omega_i t = 27$ for Case 1. In the figure, we show the distribution and $E_{\parallel}$ in the region $60d_i \leq x \leq 80d_i$. At a definite location x, the electron distribution is calculated by including all the electrons in the region 1.0 $d_i \leq z \leq 1.4d_i$, and $\bar{E}_{\parallel}$ is the averaged value in the same region. In this region, the background magnetic field

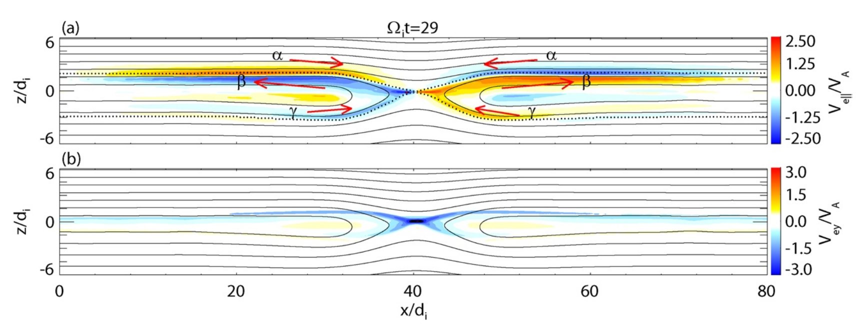

Figure 2. (a) The parallel electron bulk velocity $V_{e\parallel}$ (where $V_{e\parallel} = \boldsymbol{V}_e \cdot \boldsymbol{B}' / |\boldsymbol{B}'|$, and $\boldsymbol{V}_e$ is the electron bulk velocity). (b) The electron bulk velocity in the y direction $\boldsymbol{V}_{ey}$ at $\Omega_i t = 29$ for Case 1. Here, the dotted lines represent the separatrices. The red arrows indicate the direction of electron flows.

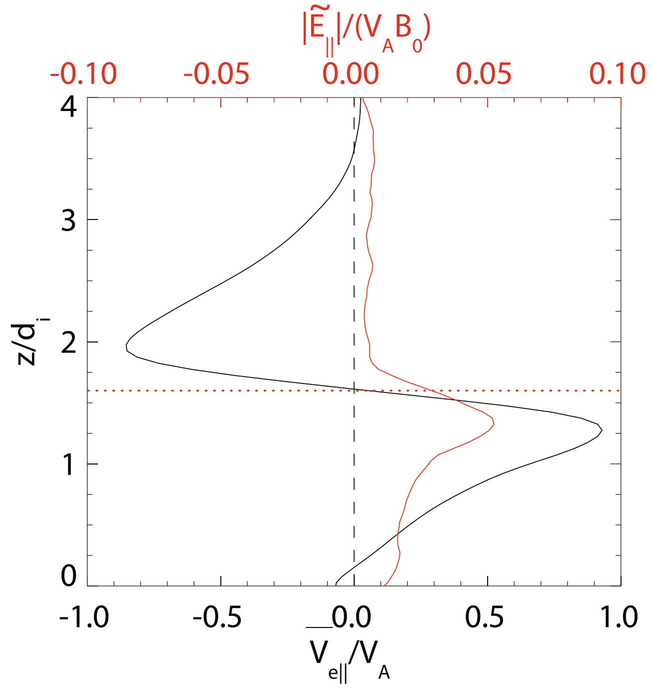

Figure 3. The distributions of $\left|\tilde{E}_{\|}\right|$ (red) and parallel electron bulk velocity $\bar{V}_{e\|}$ (black) in the region of $72\,d_i \le x \le 73.8\,d_i$ at $\Omega_i t = 29$ for Case 1.

is almost along the x direction, and we can assume that in the figure the electron distribution and parallel electric field are presented along the magnetic field lines. It is easy to identify that each bipolar structure of $E_{\|}$ correspond to a hole in the electron phase space $(x, v_{e\|})$. Therefore, we can conclude that the bipolar structure of $E_{\|}$ near the separatrices on the magnetospheric side corresponds to the BGK mode. The propagation of these structures is shown in Figure 5. Here we plot the time stacks of $E_{\|}$ along the x direction from $\Omega_i t = 25$ to $\Omega_i t = 28$. Here, $E_{\|}$ is obtained along the line $z = 1.2d_i$.These bipolar structures propagate away from the X line along the x direction. The propagating speed is about $4V_A$ in early stage, and become a little bit smaller with the time evolution.

Figure 6 shows electron and ion parallel velocity distributions $f(v_{e\|})$ and $f(v_{i\|})$ in the region $67.5\,d_i \le x \le 68.5d_i$, $1.0d_i \le z \le 1.4d_i$ for Case 1. The electron velocity distribution consists of two populations: the inflow component has the bulk velocity about $-1.5V_A$, and the outflow component has the bulk velocity about $6V_A$. In addition, a small part of electrons with the bulk velocity about $-7V_A$ is caused by the periodic boundary conditions used in the simulation. After fitting the electron distribution with a bi-Maxwellian function, we can obtain the parameters of the two electron components: the inflow component has a bulk velocity about $-1.5V_A$ and a thermal velocity about $2.4V_A$, while the outflow component has a bulk velocity about $6.5V_A$ and a thermal velocity about $1.2V_A$. The number density percentage of the outflow component and the inflow component are approximately 32% and 68%, respectively. The ion bulk velocity and thermal velocity are obtained to be about $0.1V_A$ and $1.0V_A$, respectively.

Then, based on these parameters, we can calculate the dispersion relation of the unstable modes generated by this distribution. Theoretically, the general dispersion relationship of the electrostatic instabilities with wave vector parallel to background magnetic field is:

$$D(\omega, k) = 1 + \sum_j \frac{2\omega_{pj}^2}{k^2 v_{Tj}^2}\left[1 + \zeta_j Z(\zeta_j)\right] \tag{1}$$

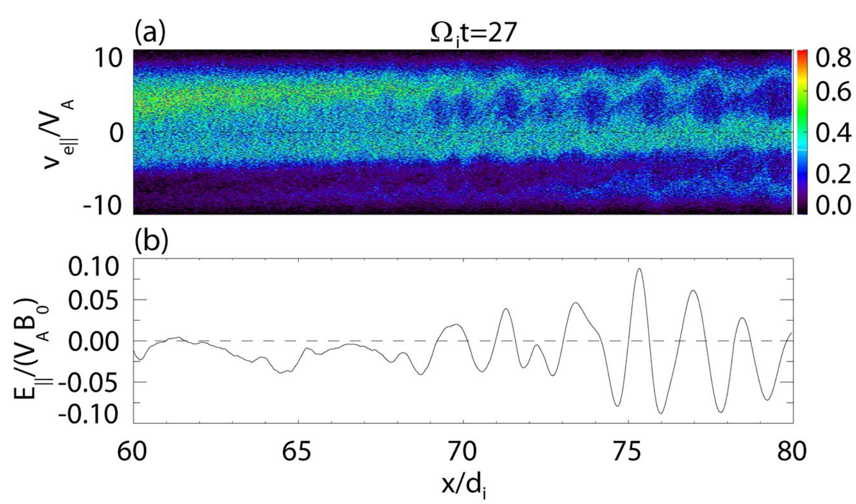

Figure 4. (a) The electron phase-space distribution versus x and $v_{e\|}$, and (b) the parallel electric field $\bar{E}_{\|}$ ($\bar{E}_{\|}$ is the averaged value of $E_{\|}$ in the region $60d_i \le x \le 80d_i$, $1.0d_i \le z \le 1.4d_i$) at $\Omega_i t = 27$ for Case 1.

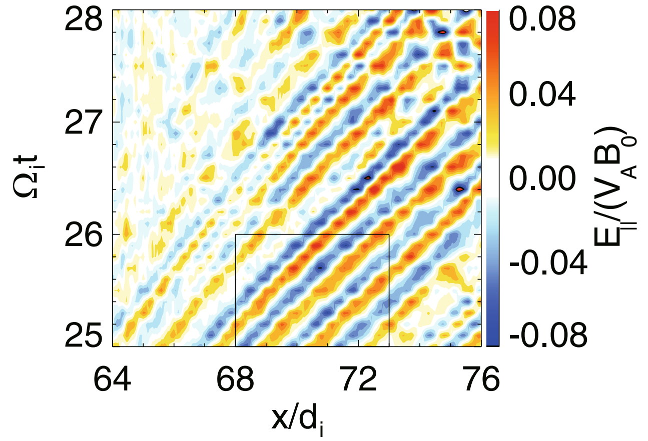

Figure 5. The time stacks of $E_{||}$ (at $z = 1.2d_i$) along the x direction from $\Omega_i t = 25$ to $\Omega_i t = 28$ for Case 1.

where $\omega = \omega_r + i\gamma$, subscripts j denote the beam component, v_{Tj} and V_j are the thermal velocity and bulk velocity of component j, respectively. ζ_j is defined as $\zeta_j = \left(\omega - \boldsymbol{k} \cdot \boldsymbol{V}_j\right) / kv_{Tj}$. Plasma dispersion function $Z\left(\zeta\right)$ is expressed as

$$Z\left(\zeta\right) = \frac{1}{\sqrt{\pi}} \int_{-\infty}^{+\infty} \frac{e^{-x^2}}{x - \zeta} dx \tag{2}$$

Figure 7 shows the wave spectrum of $E_{||}$ in the (ω, k) space for Case 1. Here, the spectrum is calculated using the Fourier transform of $E_{||}$ in the region $68d_i \le x \le 73d_i$ (at $z = 1.2d_i$) and $25\ \Omega_i^{-1} \le t \le 26\ \Omega_i^{-1}$, which is denoted by the rectangle in Figure 5. This region is chosen because the wave is in the early stage of evolution during this interval, and the linear theory can be applied. In the figure, the theoretical dispersion relation and growth rate (γ) of electron two-stream instability based on Equation 1 are also plotted for reference. We find that the power spectral density of $E_{||}$ has a peak around $\omega / \omega_{pe} \approx 0.2$ and $kd_e \approx 0.75$ (where $d_e = c / \omega_{pe}$ is the electron inertial length). The location of this peak is consistent with the theoretical dispersion relation and the wave number where the growth rate reaches maximum. Therefore, we attribute the formation of ESWs in Case 1 to the electron two-stream instability.

Now we consider the influence of the guide field, which is presented in the simulation results of Case 2. Figure 8 plots the parallel electric field $E_{||}$ at $\Omega_i t$ = (a) 16, (b) 24, (b) 34, and (d) 36 for Case 2, and the magnetic field lines are superimposed on the figure. In this case, reconnection onset occurs at about $\Omega_i t = 16$. At about $\Omega_i t = 24$, the bipolar structures of $E_{||}$ appear near the separatrices on the magnetosphere side. The parallel electric field reaches its peak amplitude at about $\Omega_i t = 34$. Different from the case without a guide field, here the amplitudes of $E_{||}$ on the right side of the X line is much stronger that those on the left side.

Figure 9 illustrates (a) the parallel electron bulk velocity $V_{e||}$ and (b) the electron bulk velocity in the y direction V_{ey} at $\Omega_i t = 34$ for Case 2. Here, the location of the electron inflow and outflow channels and the flow pattern are similar to those in Case 1. However, both the electron outflow and inflow on the right side of the X line are much stronger than those on the left side. Detailed analyses demonstrate that the bipolar structures of $E_{||}$ corresponding to electron holes range from the electron outflow channel to the inflow channel on the magnetospheric side (not shown), similar to the anti-parallel case.

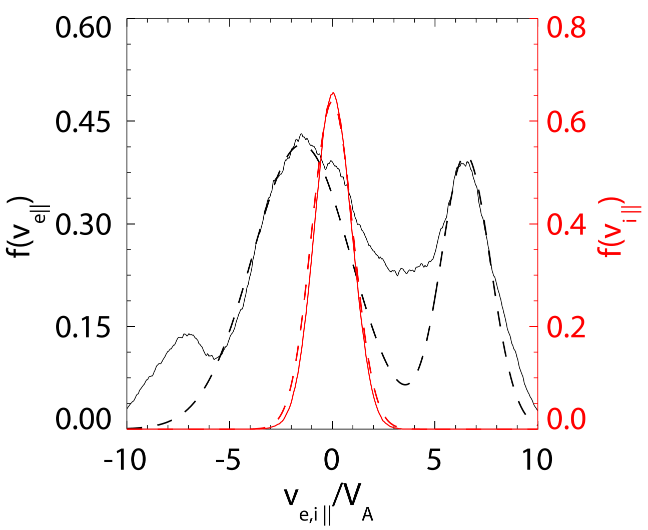

Figure 6. The electron and ion parallel velocity distributions $f(v_{e||})$ (black solid line) and $f(v_{i||})$ (red solid line) in the region $67.5\,d_i \le x \le 68.5d_i$, $1.0\,d_i \le z \le 1.4d_i$ for Case 1. The dashed line is the velocity distribution fitted by a bi-Maxwellian distribution.

Figure 10 shows the propagation of $E_{||}$ on the magnetosphere side for Case 2, which plots the time stacks of $E_{||}$ along the x direction from $\Omega_i t$ = 29.5 to $\Omega_i t$ =34 on (a) the left side of the X line ($1d_i \le x \le 16d_i$) and (b) the right side of the X line ($57d_i \le x \le 72d_i$). Here, $E_{||}$ is obtained along the line $z = 1.5d_i$. The bipolar structures of $E_{||}$ on both the left and right sides of the X line propagate away from the X line along the x direction. On the left side, similar to the anti-parallel case, there is only one kind of bipolar structures, and the propagating speed is about $2.5V_A$. On the right side, there are two kinds of bipolar structures with distinct propagating speeds, and their propagating speeds are about $1.6V_A$ and $2.4V_A$.

Figure 11 shows electron and ion parallel velocity distributions $f(v_{e||})$ and $f(v_{i||})$ in the regions (a) $10d_i \le x \le 11d_i$, $1.2d_i \le z \le 1.8\,d_i$ and (b) $57\,d_i \le x \le 58d_i$, $1.2d_i \le z \le 1.8d_i$ for Case 2. In Figure 11a, after fitting the distribution with a bi-Maxwellian function, we can obtain the parameters of the two electron components and one ion component. The inflow component has a bulk velocity about $1.3\,V_A$ and a thermal velocity about $2.2V_A$, while the outflow component has a bulk velocity about $-5.2V_A$ and

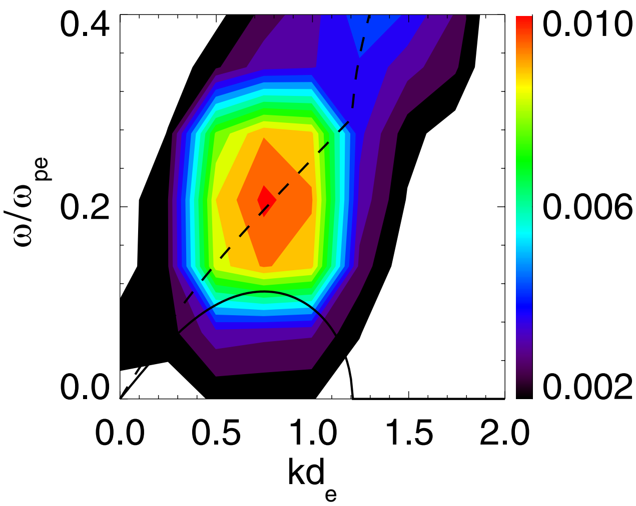

Figure 7. Wave spectrum of parallel electric field $E_{\parallel}$ in the (ω, k) space for Case 1. The sampling region is $68d_i \le x \le 73d_i$ (at $z = 1.2\, d_i$), and the time interval is $25\, \Omega_i^{-1} \le t \le 26\, \Omega_i^{-1}$, which is denoted by the rectangle in Figure 5. The black dashed and solid curves are the dispersion relation and growth rate (γ) of the electron two-stream instability calculated from the linear analyses.

a thermal velocity about $1.8V_A$. The number density percentage of the outflow component and the inflow component are approximately 55% and 45%, respectively. The ion bulk velocity and the thermal velocity are obtained to be about $-0.1V_A$ and $1.0V_A$. In Figure 11b, the electron inflow and electron outflow can be identified. In addition, a small part of electrons with the bulk velocity about $-8V_A$ is caused by the periodic boundary conditions used in the simulation. After fitting the distribution with a bi-Maxwellian function, we can obtain the parameters of the two electron components and one ion component. The inflow component has a bulk velocity about $-1.6V_A$ and a thermal velocity about $1.9V_A$, while the outflow component has a bulk velocity about $3.4V_A$ and a thermal velocity about $1.9V_A$.The number density percentage of the outflow component and the inflow component are approximately 53% and 47%, respectively. The ion bulk velocity and thermal velocity are obtained to be about 0.1 V_A and $1.0V_A$. At last, based on these parameters, we can calculate the dispersion relation of unstable modes generated by these distributions.

Figure 12 shows the wave spectrum of $E_{\parallel}$ in the (ω, k) space for Case 2. Here, the spectra in Figures 12a and 12b are calculated using the Fourier transform of $E_{\parallel}$ in the region $6d_i \le x \le 12\, d_i$, $30\, \Omega_i^{-1} \le t \le 31.5\, \Omega_i^{-1}$ and $58d_i \le x \le 65d_i$, $30\, \Omega_i^{-1} \le t \le 31.5\, \Omega_i^{-1}$ (at $z = 1.5d_i$), which are denoted by the rectangle in Figures 10a and 10b, respectively. In panel (a), the theoretical dispersion relation and growth rate (γ) of the electron two-stream instability based on Equation 1 are plotted for reference, while in panel (b), both electron two-stream instability and Buneman instability are plotted. In Figure 12a, the power spectral density of $E_{\parallel}$ has only one peak around $\omega / \omega_{pe} \approx 0.16$ and $kd_e \approx 1.0$. The phase velocity is about $2.4V_A$. The location of this peak agree well with the dispersion relation of electron two-stream instability and the wave number k where the growth rate reaches maximum. Therefore, the generation mechanism of the ESWs shown in Figure 12a is electron two-stream instability. In Figure 12b, the spectrum has two clear peaks, one appears around $\omega / \omega_{pe} \approx 0.12$ and $kd_e \approx 1.0$, and corresponding to a slower phase velocity is $1.8V_A$. The other peak is around $\omega / \omega_{pe} \approx 0.18$ and $kd_e \approx 1.2$, and the

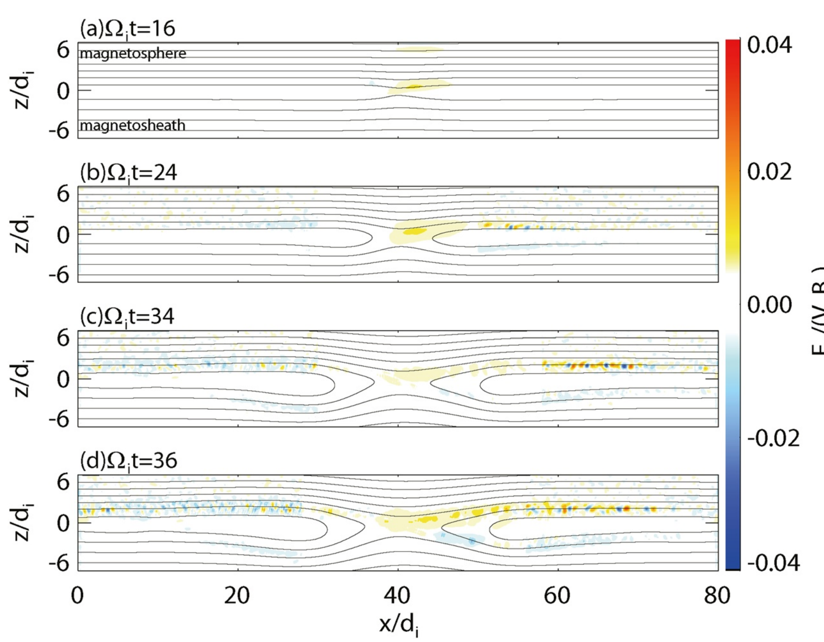

Figure 8. The parallel electric field $E_{\parallel}$ (where $E_{\parallel} = \boldsymbol{E} \cdot \boldsymbol{B}' / |\boldsymbol{B}'|$, and $\boldsymbol{B}' = B_x \boldsymbol{i}_x + B_z \boldsymbol{i}_z$ is the in-plane magnetic field) at $\Omega_i t$ = (a)16, (b)24, (b)34, and (d)36 for Case 2.

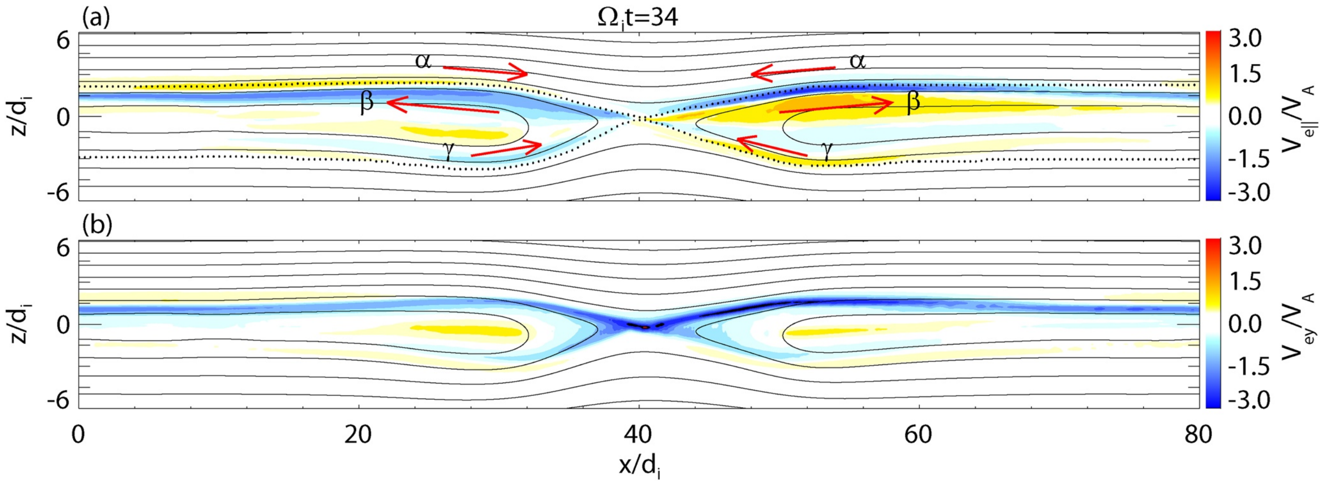

Figure 9. (a) The parallel electron bulk velocity $V_{e\|}$ (where $V_{e\|} = \boldsymbol{V}_e \cdot \boldsymbol{B}' / |\boldsymbol{B}'|$, $\boldsymbol{V}_e$ is the electron bulk velocity) and (b) the electron bulk velocity in the y direction $\boldsymbol{V}_{ey}$ at $\Omega_i t = 34$ for Case 2. Here, the dotted lines represent the separatrices.

corresponding phase velocity is $2.25V_A$. The location of the two peaks agree well with the dispersion relation of Buneman instability and electron two-stream instability, and the wave numbers k where the growth rates reach maximum. Therefore, the ESWs shown in Figure 12b are generated by both the electron two-stream instability and Buneman instability.

4. Conclusions and Discussion

In this study, we study the generation of ESWs during asymmetric magnetic reconnection with a 2-D PIC simulation model. In the simulations, we find that ESWs corresponding to electron phase-space holes can only be generated near the separatrices on the magnetosphere side, where the magnetic field is stronger and the plasma density is lower. By comparing the electrostatic structures and electron bulk velocities, we demonstrate that the position of these ESWs is near the boundary between the inflow and outflow channels of electrons, and propagate to the reconnection downstream direction along the magnetic field. When there is no guide field, the ESWs are generated by the electron two-stream instability through the nonlinear interactions between the inflow and outflow electrons. When there is a guide field, besides the ESWs generated

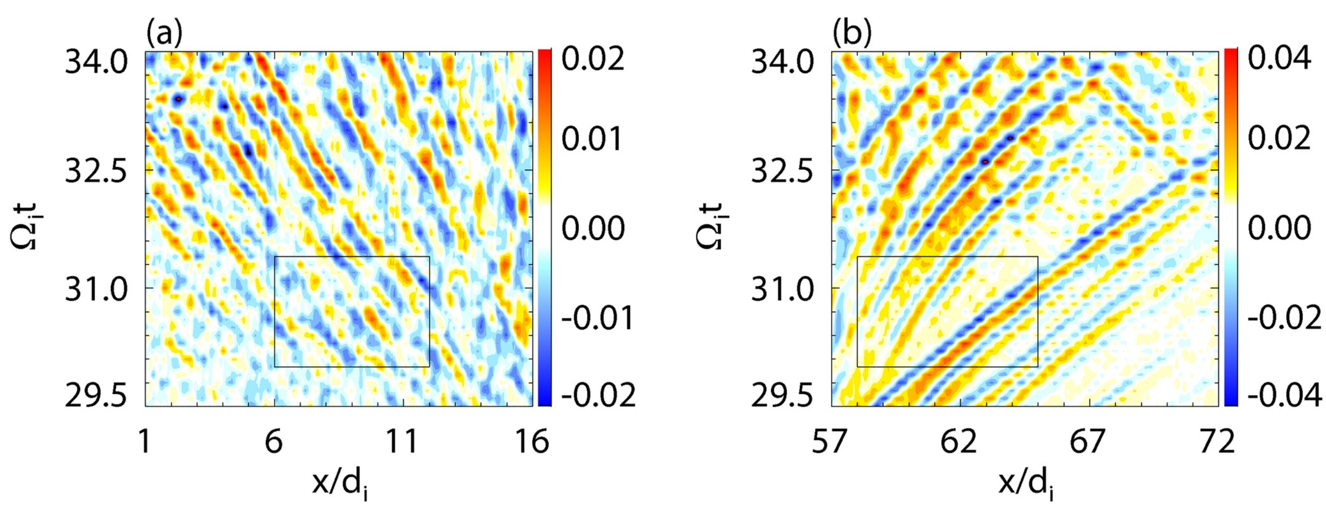

Figure 10. The time stacks of $E_\|$ (at $z = 1.5d_i$) along the x direction from $\Omega_i t = 29.5$ to $\Omega_i t = 34$ on (a) the left side of the X line ($1d_i \le x \le 16d_i$) and (b) the right side of the X line ($57d_i \le x \le 72d_i$) for Case 2.

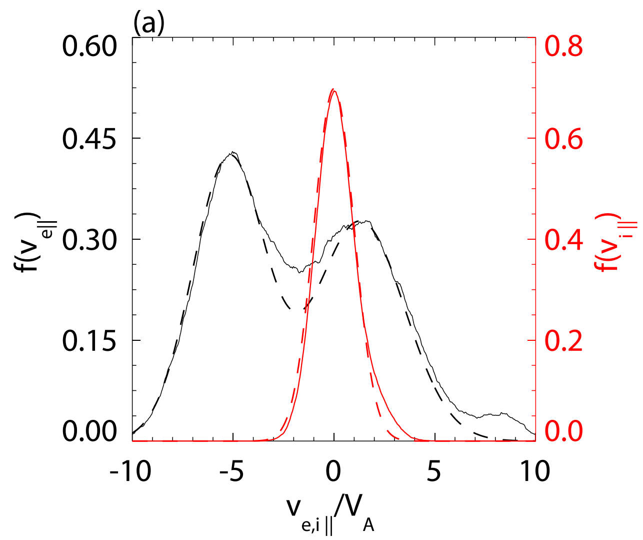

Figure 11. The electron and ion parallel velocity distributions $f(v_{e\|})$ (black solid lines) and $f(v_{i\|})$ (red solid lines) in the regions (a) $10d_i \le x \le 11d_i$, $1.2d_i \le z \le 1.8\,d_i$ and (b) $57\,d_i \le x \le 58d_i$, $1.2d_i \le z \le 1.8d_i$ for Case 2. The dashed lines are the velocity distributions fitted by bi-Maxwellian function.

by the electron two-stream instability, there still exists another kind of ESWs corresponding to the Buneman instability.

After surveying plasma waves observed by MMS satellites at asymmetric magnetic reconnection at the dayside magnetopause, Wilder et al. (2016) found that ESWs are confined in the magnetosphere side. Simultaneously, with Cluster observations, Graham et al. (2015) demonstrated the existence of two kinds of ESWs in asymmetric reconnection of the dayside magnetopause with distinct speeds and length scales. Our simulations can provide a satisfactory explanation for these observations. According to our simulations, the electron two-stream instability or Buneman instability will be responsible for the generation of ESWs near the boundary between the inflow and outflow channels of electron. The electrons from the outflow have different velocity from those from the inflow, and their relative velocity can cause the electron two-streaming instability. Simultaneously, the relative velocity between the outflow electrons and ions can cause the

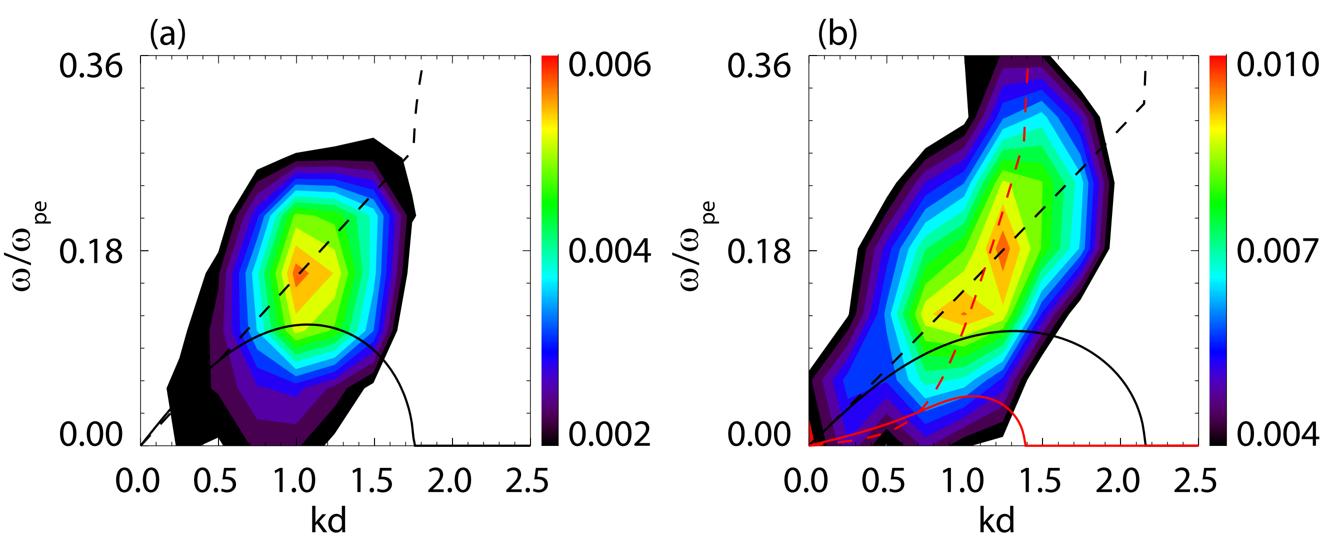

Figure 12. Wave spectrum of parallel electric field $E_\|$ (filled contours) in the (ω, k) space for Case 2. (a) The sampling region is $6d_i \le x \le 12d_i$ (at $z = 1.5d_i$), the time interval is $30\,\Omega_i^{-1} \le t \le 31.5\,\Omega_i^{-1}$ which is denoted by the rectangle in Figure 10a. (b) The sampling region is $58d_i \le x \le 65d_i$ (at $z = 1.5d_i$), and the time interval is $30\,\Omega_i^{-1} \le t \le 31.5\,\Omega_i^{-1}$, which is denoted by the rectangle in Figure 10b. The black (red) dashed and solid curves are the dispersion relation and growth rate (γ) of the electron two-stream instability (the Buneman instability) calculated from linear analyses.

excitation of the Buneman instability. In addition, we can observed both the inflow and outflow electrons on the magnetospheric side, while there only exists the electron inflow on the magnetosheath side. Therefore, we can only observe the generation of ESWs near the separatrices on the magnetosphere side, but no waves on the magnetosheath side.

In this study, we use a model where the magnetic field and plasma density across the current sheet are asymmetric while the temperature is symmetric. However, statistical studies have shown that there is typically strong temperature asymmetry in the magnetopause current sheet (Lukin et al., 2020). Using particle-in-cell simulations, Sang et al. (2019) indicated that the influence of temperature asymmetry on the in-plane current (dominated by electron flow) is much weaker than that of magnetic field and density asymmetry. Therefore, the influence of the temperature asymmetry on the generation ESWs should be negligible.

With the kinetic simulations, Lu, Artemyev, et al. (2019), Lu, Angelopoulos, et al. (2019) found that the strong temperature inhomogeneity in a current sheet further increases reconnection outflow speed, causing numerous secondary islands to be formed continuously at reconnection X-lines. Secondary islands have also been observed by satellites in different regions (Wang et al., 2010, 2016). In our study, we investigate the generation of ESWs near the separatrices in single X-line reconnection. When secondary islands are formed in the diffusion region, the electron outflow speed near the separtrices of the primary X line should be enhanced, and ESWs should be easier to be generated. However, the situation around the secondary X lines in the diffusion region should be complicated, and it is our further investigation.

In addition, Panov et al. (2011) showed that the guide field may be peaked at the magnetopause current sheet. Our simulations use a constant value of the guide field in the initial condition of the current sheet. With the development of magnetic reconnection, the magnetic field in the direction of the guided field (Hall magnetic field) has a complicated structure, and it may be a bipolar or tripolar structure with the peak at the magnetopause current sheet (Sang et al., 2019).

Data Availability Statement

The simulation data set has been uploaded to https://dx.doi.org/10.12176/01.99.00530.

Acknowledgments
This work was supported by the Strategic Priority Research Program of Chinese Academy of Sciences, Grant No. XDB 41000000, the NSFC grant 41774169, Key Research Program of Frontier Sciences, CAS (QYZDJ-SSW-DQC010), and the Fundamental Research Funds for the Central Universities WK2080000164. The data resources were supported by "National Space Science Data Center, National Science & Technology Infrastructure of China (http://www.nssdc.ac.cn)."

References

Angelopoulos, V., Artemyev, A., Phan, T. D., & Miyashita, Y. (2020). Near-Earth magnetotail reconnection powers space storms. *Nature Physics*, *16*, 317–321. https://doi.org/10.1038/s41567-019-0749-4

Angelopoulos, V., Runov, A., Zhou, X. Z., Turner, D. L., Kiehas, S. A., Li, S. S., & Shinohara, I. (2013). Electromagnetic energy conversionat reconnection fronts. *Science*, *341*(6153), 1478–1482. https://doi.org/10.1126/science.1236992

Burch, J. L., Torbert, R. B., Phan, T. D., Chen, L. J., Moore, T. E., Ergun, R. E., et al. (2016). Electron-scale measurements of magnetic reconnection in space. *Science*, *352*(6290), aaf2939. https://doi.org/10.1126/science.aaf2939

Cattell, C., Dombeck, J., Wygant, J., Drake, J. F., Swisdak, M., Goldstein, M. L., et al. (2005). Cluster observations of electron holes in association with magnetotail reconnection and comparison to simulations. *Journal of Geophysical Research*, *110*(A1), A01211. https://doi.org/10.1029/2004JA010519

Chaston, C. C., Phan, T. D., Bonnell, J. W., Mozer, F. S., Acuna, M., Goldstein, M. L., et al. (2005). Drift-kinetic Alfven waves observed near a reconnection X line in the earth's magnetopause. *Physical Review Letters*, *95*(6), 065002. https://doi.org/10.1103/PhysRevLett.95.065002

Che, H., Drake, J. F., Swisdak, M., & Yoon, P. H. (2010). Electron holes and heating in the reconnection dissipation region. *Geophysical Research Letters*, *37*(11), L11105. https://doi.org/10.1029/2010GL043608

Dokgo, K., Hwang, K. J., Burch, J. L., Choi, E., Yoon, P. H., Sibeck, D. G., & Graham, D. B. (2019). High-frequency wave generation in magnetotail reconnection: Nonlinear harmonics of upper hybrid waves. *Geophysical Research Letters*, *46*(14), 7873–7882. https://doi.org/10.1029/2019GL083361

Drake, J. F., Swisdak, M., Cattell, C., Shay, M. A., Rogers, B. N., & Zeiler, A. (2003). Formation of electron holes and particle energization during magnetic reconnection. *Science*, *299*(5608), 873–877. https://doi.org/10.1126/science.1080333

Fu, X. R., Lu, Q. M., & Wang, S. (2006). The process of electron acceleration during collisionless magnetic reconnection. *Physics of Plasmas*, *13*(1), 012309. https://doi.org/10.1063/1.2164808

Fujimoto, K. (2014). Wave activities in separatrix regions of magnetic reconnection. *Geophysical Research Letters*, *41*(8), 2721–2728. https://doi.org/10.1002/2014GL059893

Fujimoto, K., & Machida, S. (2006). A generation mechanism of electrostatic waves and subsequent electron heating in the plasma sheet–lobe boundary region during magnetic reconnection. *Journal of Geophysical Research*, *111*(A9), A09216. https://doi.org/10.1029/2005JA011542

Fujimoto, M., Shinohara, I., & Kojima, H. (2011). Reconnection and waves: A review with a perspective. *Space Science Reviews*, *160*, 123–143. https://doi.org/10.1007/s11214-011-9807-7

Genestreti, K. J., Burch, J. L., Cassak, P. A., Torbert, R. B., Ergun, R. E., Varsani, A., et al. (2017). The effect of a guide field on local energy conversion during asymmetric magnetic reconnection: MMS observations. *Journal of Geophysical Research: Space Physics*, *122*(11), 342–11. https://doi.org/10.1002/2017JA024247

Graham, D. B., Khotyaintsev, Y. V., Vaivads, A., & André, M. (2015). Electrostatic solitary waves with distinct speeds associated with asymmetric reconnection. *Geophysical Research Letters*, *42*(2), 215–224. https://doi.org/10.1002/2014GL062538

Graham, D. B., Khotyaintsev, Y. V., Vaivads, A., & André, M. (2016). Electrostatic solitary waves and electrostatic waves at the magnetopause. *Journal of Geophysical Research: Space Physics*, *121*(4), 3069–3092. https://doi.org/10.1002/2015JA021527

Graham, D. B., Vaivads, A., Khotyaintsev, Y. V., & André, M. (2016). Whistler emission in the separatrix regions of asymmetric magnetic reconnection. *Journal of Geophysical Research: Space Physics*, *121*(3), 1934–1954. https://doi.org/10.1002/2015JA021239

Huang, C., Lu, Q., Wang, P., Wu, M., & Wang, S. (2014). Characteristics of electron holes generated in the separatrix region during antiparallel magnetic reconnection. *Journal of Geophysical Research: Space Physics*, *119*(8), 6445–6454. https://doi.org/10.1002/2014JA019991

Khotyaintsev, Y. V., Vaivads, A., Andre, M., Fujimoto, M., Retino, A., & Owen, C. J. (2010). Observations of slow electron holes at a magnetic reconnection site. *Physical Review Letters*, *105*(16), 165002. https://doi.org/10.1103/PhysRevLett.105.165002

Lapenta, G., Markidis, S., Divin, A., Goldman, M., & Newman, D. (2010). Scales of guide field reconnection at the hydrogen mass ratio. *Physics of Plasmas*, *17*(8), 082106. https://doi.org/10.1063/1.3467503

Lapenta, G., Markidis, S., Divin, A., Goldman, M. V., & Newman, D. L. (2011). Bipolar electric field signatures of reconnection separatrices for a hydrogen plasma at realistic guide fields. *Geophysical Research Letters*, *38*(17), L17104. https://doi.org/10.1029/2011GL048572

Liu, C. M., Vaivads, A., Graham, D. B., Khotyaintsev, Y. V., Fu, H. S., Johlander, A., et al. (2019). Ion-beam-driven intense electrostatic solitary waves in reconnection jet. *Geophysical Research Letters*, *46*(22), 12702–12710. https://doi.org/10.1029/2019GL085419

Lotekar, A., Vasko, I. Y., Mozer, F. S., Hutchinson, I., Artemyev, A. V., Bale, S. D., et al. (2020). Multisatellite MMS analysis of electron holes in the Earth's magnetotail: Origin, properties, velocity gap, and transverse instability. *Journal of Geophysical Research: Space Physics*, *125*(9), e2020JA028066. https://doi.org/10.1029/2020JA028066

Lu, Q. M., Wang, D. Y., & Wang, S. (2005). Generation mechanism of electrostatic solitary structures in the Earth's auroral region. *Journal of Geophysical Research*, *110*(A3), A03223. https://doi.org/10.1029/2004JA010739

Lu, Q. M., Wang, S., & Dou, X. K. (2005). Electrostatic waves in an electron-beam plasma system. *Physics of Plasmas*, *12*(7), 072903. https://doi.org/10.1063/1.1951367

Lu, S., Angelopoulos, V., Artemyev, A. V., Pritchett, P. L., Liu, J., Runov, A., et al. (2019). Turbulence and particle acceleration in collisionless magnetic reconnection: Effects of temperature inhomogeneity across pre-reconnection current sheet. *The Astrophysical Journal*, *878*(2), 109. https://doi.org/10.3847/1538-4357/ab1f6b

Lu, S., Artemyev, A. V., Angelopoulos, V., Pritchett, P. L., & Runov, A. (2019). Effects of cross-sheet density and temperature inhomogeneities on magnetotail reconnection. *Geophysical Research Letters*, *46*(1), 28–36. https://doi.org/10.1029/2018GL081420

Lu, S., Lu, Q. M., Huang, C., & Wang, S. (2013). The transfer between electron bulk kinetic energy and thermal energy in collisionless magnetic reconnection. *Physics of Plasmas*, *20*(6), 061203. https://doi.org/10.1063/1.4811119

Lukin, A. S., Panov, E. V., Artemyev, A. V., Petrukovich, A. A., Haaland, S., Nakamura, R., et al. (2020). Comparison of the Flank magnetopauseat near-Earth and lunar distances: MMS and ARTEMIS observations. *Journal of Geophysical Research: Space Physics*, *125*(11), e2020JA028406. https://doi.org/10.1029/2020JA028406

Matsumoto, H., Deng, X. H., Kojima, H., & Anderson, R. R. (2003). Observation of electrostatic solitary waves associated with reconnection on the dayside magnetopause boundary. *Geophysical Research Letters*, *30*(6), 1326. https://doi.org/10.1029/2002GL016319

Omura, Y., Matsumoto, H., Miyake, T., & Kojima, H. (1996). Electron beam instabilities as generation mechanism of electrostatic solitary waves in the magnetotail. *Journal of Geophysical Research*, *101*(A2), 2685–2697. https://doi.org/10.1029/95JA03145

Panov, E. V., Artemyev, A. V., Nakamura, R., & Baumjohann, W. (2011). Two types of tangential magnetopause current sheets: Cluster observations and theory. *Journal of Geophysical Research*, *116*(A12), A12204. https://doi.org/10.1029/2011JA016860

Parker, E. N. (1957). Sweet's mechanism for merging magnetic fields in conducing fluids. *Journal of Geophysical Research*, *62*(4), 509–520. https://doi.org/10.1029/JZ062i004p00509

Pritchett, P. L. (2004). Three-dimensional collisionless magnetic reconnection in the presence of a guide field. *Journal of Geophysical Research*, *109*(A1), A01220. https://doi.org/10.1029/2003JA009999

Retinò, A., Vaivads, A., André, M., Sahraoui, F., Khotyaintsev, Y., Pickett, J. S., et al. (2006). Structure of the separatrix region close to a magnetic reconnection X-line: Cluster observations. *Geophysical Research Letters*, *33*(6), L06101. https://doi.org/10.1029/2005GL024650

Sang, L. L., Lu, Q. M., Wang, R. S., Huang, K., & Wang, S. (2018). Quadrupolar and hexapolar Hall magnetic field during asymmetric magnetic reconnection without a guide field. *Physics of Plasmas*, *25*(6), 062120. https://doi.org/10.1063/1.5030439

Sang, L. L., Lu, Q. M., Wang, R. S., Huang, K., & Wang, S. (2019). A Parametric study of the structure of hall magnetic field based on kinetic simulations. I. Anti-parallel magnetic reconnection in an asymmetric current sheet. *The Astrophysical Journal*, *877*(2), 155. https://doi.org/10.3847/1538-4357/ab14ef

Sato, T., & Hayashi, T. (1979). Externally driven magnetic reconnection and a powerful magnetic energy converter. *Physics of Fluids*, *22*(6), 1189. https://doi.org/10.1063/1.862721

Tang, X. W., Cattell, C., Dombeck, J., Dai, L., Wilson, L. B., Breneman, A., & Hupach, A. (2013). THEMIS observations of the magnetopause electron diffusion region: Large amplitude waves and heated electrons. *Geophysical Research Letters*, *40*(12), 2884–2890. https://doi.org/10.1002/grl.50565

Tong, Y., Vasko, I., Mozer, F. S., Bale, S. D., Roth, I., Artemyev, A. V., et al. (2018). Simultaneous multispacecraft probing of electron phase space holes. *Geophysical Research Letters*, *45*(21), 11513–11519. https://doi.org/10.1029/2018GL079044

Vaivads, A., Khotyaintsev, Y., Andre, M., Retino, A., Buchert, S. C., Rogers, B. N., et al. (2004). Structure of the magnetic reconnection diffusion region from four-spacecraft observations. *Physical Review Letters*, *93*(10), 105001. https://doi.org/10.1103/PhysRevLett.93.105001

Viberg, H., Khotyaintsev, Y. V., Vaivads, A., André, M., & Pickett, J. S. (2013). Mapping HF waves in the reconnection diffusion region. *Geophysical Research Letters*, *40*(6), 1032–1037. https://doi.org/10.1002/grl.50227

Wang, R., Lu, Q., Du, A., & Wang, S. (2010). In situ observations of a secondary magnetic island in an ion diffusion region and associated energetic electrons. *Physical Review Letters*, *104*(17), 175003. https://doi.org/10.1103/PhysRevLett.104.175003

Wang, R., Lu, Q., Nakamura, R., Huang, C., Du, A., Guo, F., et al. (2016). Coalescence of magnetic flux ropes in the ion diffusion region of magnetic reconnection. *Nature Physics*, *12*(3), 263–267. https://doi.org/10.1038/nphys3578

Wang, S., & Lu, Q. M. (2019). *Collisionless magnetic reconnection*. Beijing: Science Press.

Webster, J. M., Burch, J. L., Reiff, P. H., Daou, A. G., Genestreti, K. J., Graham, D. B., et al. (2018). Magnetospheric multiscale dayside reconnection electron diffusion region events. *Journal of Geophysical Research: Space Physics*, *123*(6), 4858–4878. https://doi.org/10.1029/2018JA025245

Wilder, F. D., Ergun, R. E., Goodrich, K. A., Goldman, M. V., Newman, D. L., Malaspina, D. M., et al. (2016). Observations of whistler mode waves with nonlinear parallel electric fields near the dayside magnetic reconnection separatrix by the magnetospheric multiscale mission. *Geophysical Research Letters*, *43*(12), 5909–5917. https://doi.org/10.1002/2016GL069473

Wilder, F. D., Ergun, R. E., Newman, D. L., Goodrich, K. A., Trattner, K. J., Goldman, M. V., et al. (2017). The nonlinear behavior of whistler waves at the reconnecting dayside magnetopause as observed by the Magnetospheric Multiscale mission: A case study. *Journal of Geophysical Research: Space Physics*, *122*(5), 5487–5501. https://doi.org/10.1002/2017JA024062

Yamada, M., Kulsrud, R., & Ji, H. T. (2010). Magnetic reconnection. *Reviews of Modern Physics*, *82*(1), 603–664. https://doi.org/10.1103/RevModPhys.82.603

Zhang, X., Angelopoulos, V., Artemyev, A. V., & Liu, J. (2019). Energy transport by Whistler waves around dipolarizing flux Bundles. *Geophysical Research Letters*, *46*(21), 11718–11727. https://doi.org/10.1029/2019GL084226

Zhou, M., Deng, X. H., Li, S. Y., Pang, Y., Vaivads, A., Rème, H., et al. (2009). Observation of waves near lower hybrid frequency in the reconnection region with thin current sheet. *Journal of Geophysical Research*, *114*(A2), A02216. https://doi.org/10.1029/2008JA013427